



Synthesis and electrochemical characteristics of NASICON-structured $\text{LiSn}_2(\text{PO}_4)_3$ anode material for lithium-ion batteries

Wang-Jun Cui, Jin Yi, Long Chen, Cong-Xiao Wang, Yong-Yao Xia*

Department of Chemistry and Shanghai Key Laboratory of Molecular Catalysis and Innovative Materials, Institute of New Energy, Fudan University, Shanghai 200433, China

HIGHLIGHTS

- The NASICON-structured $\text{LiSn}_2(\text{PO}_4)_3$ was prepared through a solid-state reaction.
- This material exhibits better cycling performance than SnO_2 .
- The lithiation mechanism was confirmed by ex-situ XRD and EIS tests.
- The improved cycling performance is due to the well formed Li_3PO_4 matrix.

ARTICLE INFO

Article history:

Received 26 March 2012

Received in revised form

11 May 2012

Accepted 31 May 2012

Available online 9 June 2012

Keywords:

Tin-based anode
Lithium phosphate
Lithium-ion battery
Solid-state reaction
Thermal stability

ABSTRACT

Li_3PO_4 , with a Li ion conductivity of $8.62 \times 10^{-8} \text{ S cm}^{-1}$, is considered as a matrix material in this study to improve the cyclability of tin anodes. Toward this goal, a well-crystallized NASICON-structured $\text{LiSn}_2(\text{PO}_4)_3$ using nano- SnO_2 as a precursor has been prepared at 900°C using a solid-state reaction. Compared to SnO_2 , this material exhibits better cycling performance, with a capacity of 320 mAh g^{-1} after 50 cycles. Additionally, the insertion/extraction mechanism of $\text{LiSn}_2(\text{PO}_4)_3$ is investigated through ex-situ X-ray diffraction (XRD) and electrochemical impedance spectroscopy (EIS) measurements. The apparent diffusion coefficient (D_{Li}) is studied using cyclic voltammetry (CV) experiments employing a powder microelectrode. In addition, differential scanning calorimetry (DSC) measurements are employed to investigate the thermal stability of $\text{LiSn}_2(\text{PO}_4)_3$.

© 2012 Elsevier B.V. All rights reserved.

1. Introduction

Tin-based materials have been demonstrated to be a promising alternative to carbon for use as a negative-electrode material because of their high theoretical capacity of 990 mAh g^{-1} , as compared to 372 mAh g^{-1} for graphite. However, the one major problem that prevents their use in commercial applications is that they undergo large volume changes during cycling, which results in disintegration of the electrodes and subsequent rapid capacity fading [1–4]. One of the effective strategies is to finely disperse tin into an inactive matrix. This matrix can be an electronic conductive metal, M, or ionic conductive materials such as Li_2O and Li_2S . The lithium alloying reaction typically occurs as follows:



where M is a metallic element, for example, Cu or Co



where M' is a nonmetallic element, for example, O or S. The “inactive phase M' ” is mainly to play the role of a “matrix-glue” to hold the particles together and to provide a matrix that will absorb the massive volume changes occur within the electrode during the lithiation (expansion)/delithiation (contraction) process, thereby improving the cycling performance of the anode material compared to pure Sn.

Based on this principle, many types of “Sn/matrix” systems have been investigated in recent years, such as tin composite oxide (TCO) glasses [5,6], SnSO_4 [7], Sn-Co-C [8,9], SnS_2 [10], Cu_6Sn_5 [11] and CoSn [12]. The results from these works show that the matrix has a great effect on the electrochemical performance of tin composites.

In SnO_2 , the Li_2O matrix formed during the first discharging cycle definitely binds, to some extent, the lithium–tin regions together and smoothes the large volume changes associated with alloying and dealloying during reversible charge and discharge reactions [13,14]. The situation in chlorides and sulfides is almost

* Corresponding author. Tel./fax: +86 21 51630318.

E-mail address: yyxia@fudan.edu.cn (Y.-Y. Xia).

the same, and Li_2S seems to be a better matrix material than Li_2O because of the higher Li ion conductivity. However, capacity fading upon cycling is still observed, which is most likely caused by the aggregation of tin atoms into clusters with the growth in size [15,16].

It is suggested that a proper matrix should keep the tin well dispersed during cycling while simultaneously having good Li ion conductivity. Li_3PO_4 , which has a Li ion conductivity of $8.62 \times 10^{-8} \text{ S cm}^{-1}$, is a promising matrix material with better properties than Li_2O . Recent work reported by Lu's group shows improved cyclability of $\text{LiGe}_2(\text{PO}_4)_3$ compared to GeO_2 [17]. $\text{LiGe}_2(\text{PO}_4)_3$ possesses a reversible capacity of 460 mAh g^{-1} at a charge/discharge rate of 150 mA g^{-1} and a good capacity retention of 92% after 25 cycles, compared to 28% for GeO_2 . These results suggest that Li_3PO_4 should be a more stable conductive matrix than Li_2O for buffering the volume expansion during the Li-alloy process. However, according to Irvine's work, the Li_3PO_4 used in tin phosphate-based anodes showed unsatisfying performance [18].

In this work, which focuses on improving the electrochemical performance of tin phosphate, a systematic study of the synthesis and electrochemistry process of $\text{LiSn}_2(\text{PO}_4)_3$ was presented. The NASICON-structured $\text{LiSn}_2(\text{PO}_4)_3$, which has good cyclability when using nano- SnO_2 as precursor, was prepared using a solid-state reaction. Additionally, the insertion/extraction mechanism and the thermal stability of $\text{LiSn}_2(\text{PO}_4)_3$ were investigated through ex-situ X-ray diffraction (XRD) measurements and differential scanning calorimetry (DSC) measurements.

2. Experimental

2.1. Chemicals

Tin chloride hydrate ($\text{SnCl}_4 \cdot 5\text{H}_2\text{O}$, 98%), lithium carbonate anhydrous (Li_2CO_3 , 98%), diammonium hydrogen phosphate ($(\text{NH}_4)_2\text{HPO}_4$, >98%) and ethanol were analytical reagents purchased from the Shanghai Chemical Company. All chemicals were used as received without further purification. Deionized water was used in all experiments.

2.2. Synthesis

The nano- SnO_2 precursor was prepared according to a reported hydrothermal method [19]. A solid-state method was used to prepare $\text{LiSn}_2(\text{PO}_4)_3$. Stoichiometric amounts of Li_2CO_3 , nano- SnO_2 , and $(\text{NH}_4)_2\text{HPO}_4$ were thoroughly mixed and calcined in an aluminum oxide crucible at various temperatures between 700°C and 1000°C in air for 10 h. The obtained powder was ground before each measurement.

2.3. Characterization

The particle morphologies and sizes were characterized using a JEOL JSM6390 scanning electron microscope (SEM). For the SEM examination of the electrodes following charge/discharge, the electrode films were washed using dimethyl carbonate (DMC) and then dried in a vacuum at room temperature prior to characterization [20,21]. Thermogravimetric (TG) measurements and differential thermal analysis (DTA) was performed using a Perkin–Elmer TGA 7 thermal analyzer at a heating rate of $10^\circ\text{C min}^{-1}$ in a 40 mL min^{-1} flow of air. X-ray diffraction (XRD) patterns were recorded on a Bruker D8 X-ray diffractometer at a scan rate of $0.2^\circ \text{ deg sec}^{-1}$ using $\text{Cu K}\alpha$ radiation ($\lambda = 1.5406 \text{ \AA}$).

The changes in the crystal structure of $\text{LiSn}_2(\text{PO}_4)_3$ during charge/discharge were investigated using ex-situ X-ray diffraction. The air-sensitive samples, at various charged states, were prepared

inside a glove box by carefully opening the cells and then placing the products onto a glass sample-holder with an Al foil covering. The diffraction patterns were recorded under dynamic vacuum to avoid undesirable reactions with air. The obtained XRD data were analyzed using the Material Data Jade 5.0 software.

2.4. Electrochemical tests

Electrochemical tests were performed in a CR2016-type coin cell. Metallic lithium was used as the negative electrode. The working electrodes were prepared by mixing 80% sample powders, 10% carbon black, and 10% polyvinylidene fluoride (PVDF) dissolved in N-methylpyrrolidinone (NMP). The slurries of the mixture were applied to a Cu foil. After coating, the electrodes were dried at 80°C for 10 min to remove the solvent before pressing. The electrodes were cut into sheets 1 cm^2 in area, vacuum-dried at 100°C for 24 h and then weighed before assembly. The typical mass load of the active material was approximately 8 mg cm^{-2} . The cell assembly was operated in a glove box (model 100G, MBraun, Germany) filled with pure argon that had a moisture and oxygen pressure below 0.1 ppm. The electrolyte solution was 1 M LiPF_6 /ethylene carbonate (EC)/dimethyl carbonate (DMC)/diethyl carbonate (DEC) (1:1:1 by volume). The cells were assembled with the as-prepared cathodes, lithium metal anodes, and separators made from a Celgard 2300 film. The charge–discharge experiments were performed using a constant current density of 100 mA g^{-1} between 2.0 V and 0.0 V with a LAND CT2001A Battery Cycler (Wuhan, China). Lithium insertion into the working electrode was referred to as discharge, and the extraction was referred to as charge. The cell capacity was determined by only the active material.

Lithium-ions transfer at the interface between the electrode and electrolyte was investigated using electrochemical impedance spectroscopy (EIS) measurements in a three-electrode cell. The experiment was using a Solartron Instrument model no.1287 electrochemical interface and 1255B frequency response analyzer in the frequency range between 1000 kHz and 0.01 Hz at different lithium intercalation states. The AC oscillation was 5 mV, and all of the tests were performed at 25°C . The cell was charged or discharged to a given potential at 0.25°C (100 mA g^{-1}). Then, the potential was maintained for 2 h to fully reduce polarization before testing [22].

Cyclic voltammetry experiments were performed using a powder microelectrode to evaluate the apparent diffusion coefficient of the Li ion (D_{Li}) at 25°C . The preparation of the powder microelectrode which contains a groove with a diameter of $100 \mu\text{m}$ and $5 \mu\text{m}$ in depth was described in our previous work [23]. Before the electrochemical tests, the prepared powder microelectrode was compacted with the electrode material powder ($\text{LiSn}_2(\text{PO}_4)_3$) by grinding for 15 min to serve as a working electrode. Lithium-metal foils were used as the counter and reference electrodes. The electrolyte solution was 1 M LiPF_6 /ethylene carbonate (EC)/dimethyl carbonate (DMC)/diethyl carbonate (DEC) (1:1:1 by volume). The cell was assembled into a glass container inside of an argon-filled glove box for the cyclic voltammetry tests. The series of experiments were conducted using different scan rates with a Solartron Instrument model 1287 controlled by a computer.

2.5. Thermal stability tests

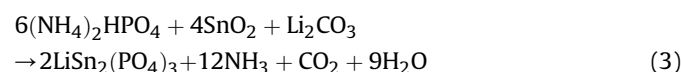
For the DSC (Differential Scanning Calorimetry) measurements, the cells were cycled 5 times to reach a stable capacity and ended at 0 V when the cathode discharged to a fully lithiated state. The cells were disassembled in a glove box. Approximately 2 mg of the electrode materials were scraped from the copper current-collector without removing the electrolyte. The obtained materials along

with the same amount of electrolyte were transferred and sealed into a high-pressure stainless-steel pan with a gold-plated copper seal. The DSC scans were performed using a DSC 200 F3 instrument (NETZSCH, Germany) with a scanning rate of $10\text{ }^{\circ}\text{C min}^{-1}$. The weights of DSC pans were measured before and after the DSC measurements to guarantee that there was no leakage during the experiment [24].

3. Results and discussion

3.1. Structural and chemical characterization of $\text{LiSn}_2(\text{PO}_4)_3$

To investigate the effect of the heat-treatment temperature on the synthesis of $\text{LiSn}_2(\text{PO}_4)_3$, the TG/DTA curve was recorded from a mixture of stoichiometric amounts of SnO_2 , $(\text{NH}_4)_2\text{HPO}_4$, and Li_2CO_3 , as shown in Fig. 1. The TG curve shows a soft slope before $200\text{ }^{\circ}\text{C}$ and a steep slope in the range of $200\text{--}600\text{ }^{\circ}\text{C}$, with a weight loss of 27.0%. According to the reaction Eq. (3), the formation of $\text{LiSn}_2(\text{PO}_4)_3$ from stoichiometric amounts of SnO_2 , $(\text{NH}_4)_2\text{HPO}_4$, and Li_2CO_3 must be accompanied by an overall weight loss of 27.9%, which is in good agreement with the experiment results.



At temperatures above $600\text{ }^{\circ}\text{C}$, there was no significant weight loss, which suggests that the gases (NH_3 , CO_2 and H_2O) are mainly produced below $600\text{ }^{\circ}\text{C}$ and that the reaction at high temperature does not result in further weight loss. Three distinct endothermic peaks are observed in the DTA curve. Taking into account the possible reactions that occur during the heating process, the peak at $190\text{ }^{\circ}\text{C}$ can be attributed to the decomposition of $(\text{NH}_4)_2\text{HPO}_4$, and the peaks at $555\text{ }^{\circ}\text{C}$ and $870\text{ }^{\circ}\text{C}$ can be ascribed to the formation of SnP_2O_7 and $\text{LiSn}_2(\text{PO}_4)_3$, respectively [25].

The phase composition of $\text{LiSn}_2(\text{PO}_4)_3$ prepared at different temperatures was determined from X-ray diffraction analysis. Fig. 2a–d show the X-ray diffraction patterns of $\text{LiSn}_2(\text{PO}_4)_3$ synthesized at various temperatures, for 10 h using a typical solid-state method. These figures show that all of the patterns have the same peaks at $2\theta = 14.5^\circ$, 19.9° , 21.1° , 24.2° , 29.3° , 32.1° , and 36.2° , which can be indexed to crystalline $\text{LiSn}_2(\text{PO}_4)_3$ (JCPDS 49–1175, phase I) with a NASICON-type structure and monoclinic Cc symmetry. At a low synthesis temperature of $700\text{ }^{\circ}\text{C}$, the lower intensity of the main peaks indicates low crystallinity of the $\text{LiSn}_2(\text{PO}_4)_3$ particles. In addition, the peaks of $\text{LiSn}_2(\text{PO}_4)_3$ appear

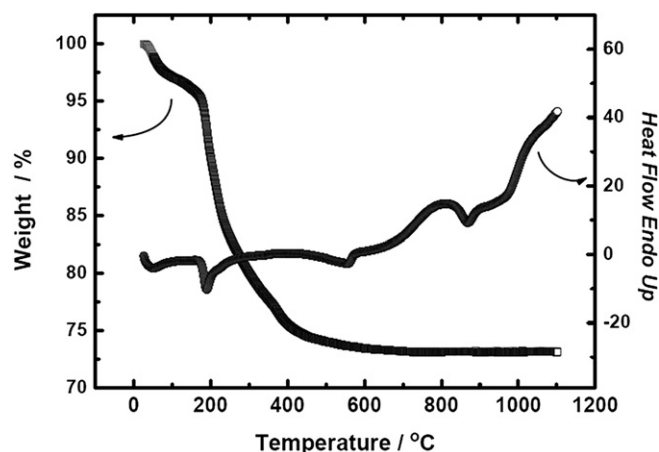


Fig. 1. The TG/DTA curve recorded from a mixture of stoichiometric amounts of SnO_2 , $(\text{NH}_4)_2\text{HPO}_4$, and Li_2CO_3 , in air flow at a heating rate of $10\text{ }^{\circ}\text{C min}^{-1}$.

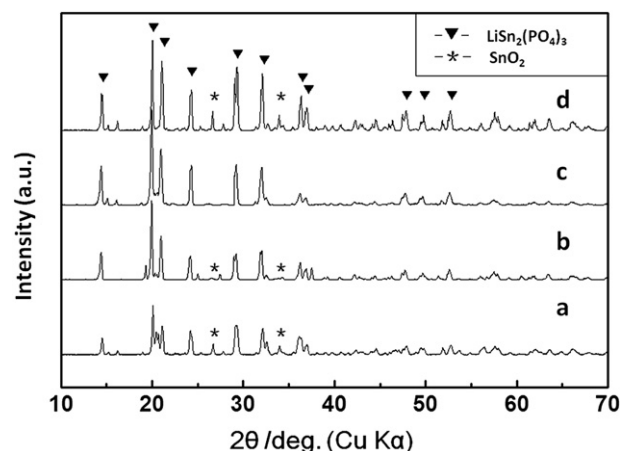


Fig. 2. X-ray diffraction patterns of $\text{LiSn}_2(\text{PO}_4)_3$ synthesized at $700\text{ }^{\circ}\text{C}$, $800\text{ }^{\circ}\text{C}$, $900\text{ }^{\circ}\text{C}$ and $1000\text{ }^{\circ}\text{C}$ using a typical solid-state method. (a. $700\text{ }^{\circ}\text{C}$, b. $800\text{ }^{\circ}\text{C}$, c. $900\text{ }^{\circ}\text{C}$, d. $1000\text{ }^{\circ}\text{C}$).

along with some impurities. The impurity peaks at 20.3° and 20.6° can be assigned to another $\text{LiSn}_2(\text{PO}_4)_3$ NASICON-structure (JCPDS 87–2078, phase II) with rhombohedral $R3c$ symmetry, and the peaks at 26.6° and 33.9° can be indexed to unreacted cassiterite SnO_2 (JCPDS 77–0447). It has previously been reported that SnO_2 and the two phases of $\text{LiSn}_2(\text{PO}_4)_3$ coexist at temperatures below $700\text{ }^{\circ}\text{C}$, and at temperatures above $700\text{ }^{\circ}\text{C}$, phase II gradually transforms to phase I [26]. Fig. 2b and c clearly show that the intensity of the phase I peaks increased with the decrease of phase II in both samples. A slight impurity of SnO_2 still exists at $800\text{ }^{\circ}\text{C}$. When the temperature is increased to $900\text{ }^{\circ}\text{C}$, a pure, well-crystallized NASICON structure is obtained. After further increasing the temperature to $1000\text{ }^{\circ}\text{C}$, an extra second phase, SnO_2 , emerges because of the Li loss at high temperature, as shown in Fig. 2d. Therefore, to obtain the pure phase of $\text{LiSn}_2(\text{PO}_4)_3$, the appropriate synthesis temperature is $900\text{ }^{\circ}\text{C}$.

Fig. 3 shows the SEM images of the $\text{LiSn}_2(\text{PO}_4)_3$ synthesized at various temperatures. The difference in particle sizes can be easily observed from the morphology images. At $700\text{ }^{\circ}\text{C}$ and $800\text{ }^{\circ}\text{C}$, the samples obviously consist of small particles with rough surfaces, which are not fully crystallized because of the relatively low synthesis temperature. Nevertheless, the sample prepared at $900\text{ }^{\circ}\text{C}$ reveals partly agglomerated particles that have well-shaped, smooth surfaces with clear edges. The primary particle size ranges from 0.5 to $1\text{ }\mu\text{m}$, which is in agreement with the sizes calculated from the XRD patterns using the Scherrer formula: $D = K\lambda/\beta\cos\theta$. Additionally, when the synthesis temperature is increased to $1000\text{ }^{\circ}\text{C}$, the particles show clear edges and corners with the particle size dramatically increasing to $2\text{--}5\text{ }\mu\text{m}$. The large grains in this size may cause considerable polarization during the charge/discharge process. The results suggest that the sample morphology is highly dependent on the synthesis temperature. Taking the size factor into consideration, the optimal synthesis temperature is $900\text{ }^{\circ}\text{C}$.

3.2. Electrochemical performance and lithiation mechanism of $\text{LiSn}_2(\text{PO}_4)_3$

The charge/discharge profiles of $\text{LiSn}_2(\text{PO}_4)_3$ and nano- SnO_2 are shown in Fig. 4a and b, respectively, and the cycling test profiles are shown as insets in each of the figures. As demonstrated in Fig. 4a, a clear plateau appears at approximately 1.2 V and ends at approximately 1.0 V , with a discharge capacity of 415 mAh g^{-1} during the first cycle. The theoretical capacity of this

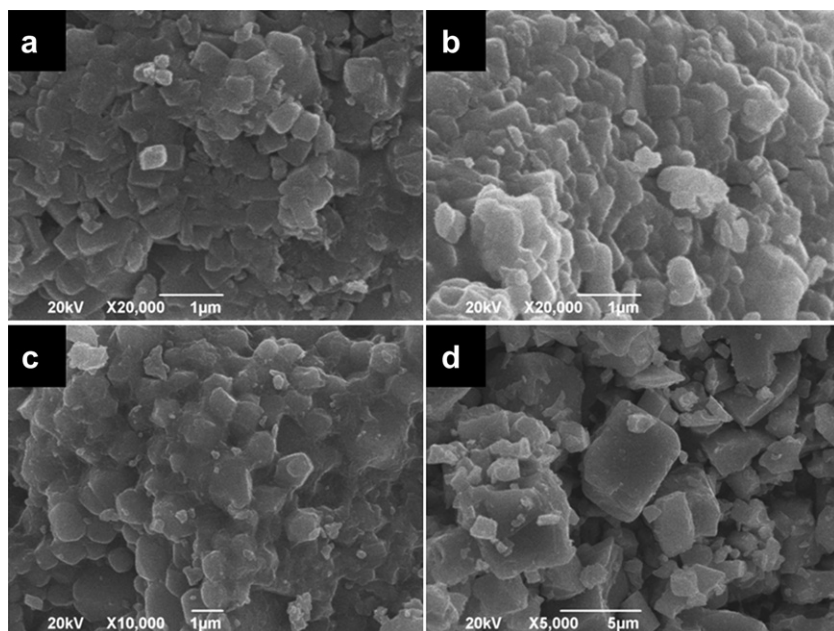


Fig. 3. SEM images of the $\text{LiSn}_2(\text{PO}_4)_3$ obtained at various temperatures. (a. 700 °C, b. 800 °C, c. 900 °C, d. 1000 °C).

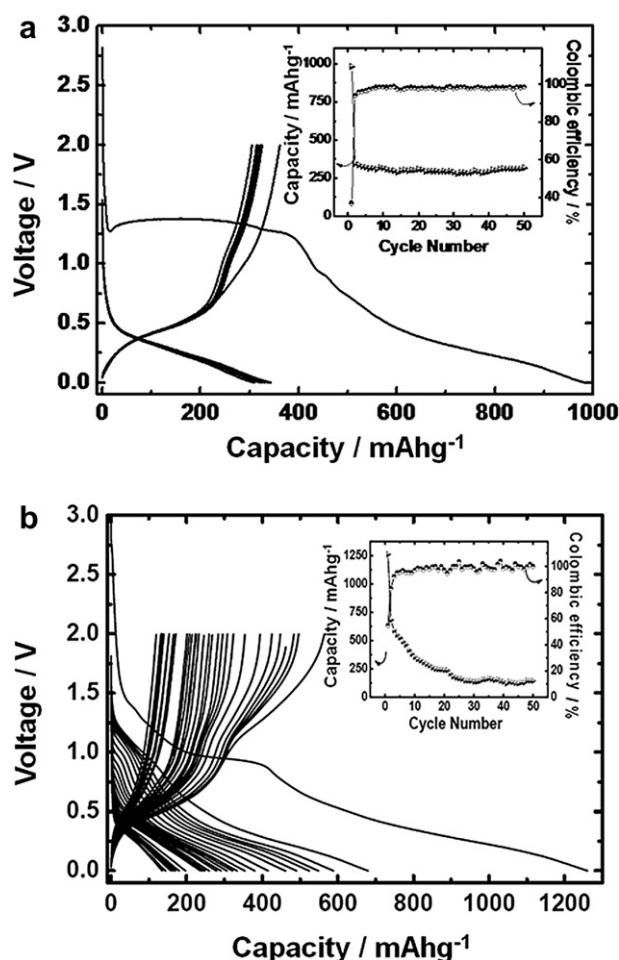
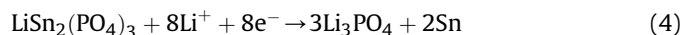


Fig. 4. The charge/discharge profiles of a) $\text{LiSn}_2(\text{PO}_4)_3$ and b) nano- SnO_2 in a voltage range between 2.0 V and 0.0 V for 50 cycles. (The cycling test profiles are shown in each figures as insets.).

transformation should be 410 mAh g^{-1} according to Eq. (4), which is consistent with our result.



Because the solid electrolyte interface (SEI) film will not form in this voltage range, this plateau can be ascribed to the irreversible reduction of Sn(IV) to Sn(0) accompanied with the formation of Li_3PO_4 . It is noteworthy that a minimum voltage is obtained at the beginning of the plateau, which is in good agreement with the findings of Irvine's work where the electronic conductivity is improved as tin metal begins to form and is believed responsible for this phenomenon [18]. Additionally, a sloping discharge/charge behavior with a capacity of 605 mAh g^{-1} is obtained when the voltage ranges from 1.0 V to 0.0 V. This corresponds to the sequential partial reversible Li^+ ion insertion that will terminate until the full lithiation $\text{Li}_{4.4}\text{Sn}$ is reached. Additionally, a capacity of 162 mAh g^{-1} that exceeds the theoretical capacity in this region can undoubtedly be ascribed to the SEI formation. After the first discharge, the electrochemical process, which is shown as sloping lines in the figure, is mainly dependant on the reaction of the reversible lithiation of Sn. The capacity and the coulombic efficiency versus cycle numbers are plotted in the inset of Fig. 4a. Starting at the second cycle, $\text{LiSn}_2(\text{PO}_4)_3$ exhibits good cycling performance with a capacity of 320 mAh g^{-1} after 50 cycles, with the capacity retention maintained above 85%.

Fig. 4b shows the charge/discharge profiles of nano-scale SnO_2 , which exhibits a sloping discharge/charge behavior with an initial discharge capacity of 1230 mAh g^{-1} and charge capacity of 600 mAh g^{-1} . However, this material exhibits poor cycling performance. The capacity and the coulombic efficiency versus cycle numbers are plotted in the inset of Fig. 4b. Nano-sized SnO_2 , using a Li_2O matrix during charge/discharge, delivers a capacity of only 110 mAh g^{-1} and shows an 82% loss from the first charge capacity after 50 cycles, which is caused by the aggregation of nanoparticles and the formation of inactive tin clusters during subsequent cycling [27]. The coulombic efficiency of the nano-sized SnO_2 increases from 49% in the first cycle to 99% in the 50th cycle, which indicates that the irreversible capacity from the formation of a large amount

of surface solid electrolyte interface (SEI) film mainly affects the first cycle. This is because of the large surface area of the nano-scale material and the reaction with functional groups that exist on the particle surface after the low-temperature synthesis process [28]. The decay of other cycles is attributed to alloy aggregation and pulverization.

In general, $\text{LiSn}_2(\text{PO}_4)_3$ demonstrates good cycling stability compared to that of the nano-sized SnO_2 . The distinct difference in cyclability between these two compounds is mainly due to the different matrix materials. As mentioned above, it can therefore be concluded that the electrochemical processes of highly dispersed nano-Sn particles in Li_3PO_4 matrices formed in $\text{LiSn}_2(\text{PO}_4)_3$ are more stable than in the Li_2O matrix formed in SnO_2 . In addition, the high reversibility also benefits from the high Li ionic diffusion rate of $\text{LiSn}_2(\text{PO}_4)_3$ and Li_3PO_4 compared with SnO_2 and Li_2O because high Li ionic diffusion rates make the lithiation of the $\text{LiSn}_2(\text{PO}_4)_3$ particles much easier [29,30].

The surface morphologies of the prepared $\text{LiSn}_2(\text{PO}_4)_3$ electrode film following several charge and discharge cycles were investigated using SEM, as shown in Fig. 5. Before discharge, the $\text{LiSn}_2(\text{PO}_4)_3$ particles are clearly visible, and they are all surrounded and connected by carbon black and the binder. However, as shown in Fig. 5b, after 2 cycles, a thin film is formed on the surface of the active material particles that fills the gap between them and makes the particles smoother and tighter. This effect becomes more significant as the number of cycles is increased, as shown in Fig. 5c and d. After 50 cycles, an even smoother surface is formed and exhibits no cracks, which is very different from the reported results obtained for tin oxides [17]. This result indicates that the compact Li_3PO_4 matrix has formed and that this matrix is so stable during the charge and discharge cycles that the tin volume expansion during lithiation can be effectively alleviated to obtain improved cyclability.

Ex-situ XRD experiments were used to confirm the Li reaction mechanisms of $\text{LiSn}_2(\text{PO}_4)_3$. The cell was discharged at 100 mA g^{-1} to 0.0 V for the first cycle. The results obtained during the first cycle of a $\text{Li}/\text{LiSn}_2(\text{PO}_4)_3$ cell at OCV (open circuit voltage), 1.0 V and 0.0 V are presented in Fig. 6a–c, respectively. As shown in Fig. 6a, the

undischarged electrode exhibits clear peaks for the crystallized $\text{LiSn}_2(\text{PO}_4)_3$ (JCPDS 49-1175, the peaks at $2\theta = 43.3^\circ$, 50.4° and 74.1° can be indexed to the copper current collector.) As shown in Fig. 6b, when the cell is discharged to 1.0 V, the intensity of the diffraction peaks of $\text{LiSn}_2(\text{PO}_4)_3$ is greatly reduced, which suggests the transformation of $\text{LiSn}_2(\text{PO}_4)_3$ to Li_3PO_4 . A small peak at 22.20° corresponds to Li_3PO_4 (JCPDS 45 0747), according to previously reported work [16], and the low density is probably due to the low crystallization and the small sizes of the formed Li_3PO_4 . Additionally, the patterns from the electrode that was discharged to 0.0 V, as shown in Fig. 6c, show no sharp peaks; instead, these patterns show broad peaks between 22° and 24° , which are ascribed to the product of amorphous Li_3PO_4 and Li_xSn . These results provide clear evidence that the insertion of lithium ions into $\text{LiSn}_2(\text{PO}_4)_3$ results in the complete destruction of the materials' crystallinity. This phenomenon is in agreement with the results of many tin-based glass systems [31,32], and the large irreversible capacity during first discharge is caused by this matrix formation reaction.

The ex-situ XRD patterns of the cycled $\text{LiSn}_2(\text{PO}_4)_3$ electrode after 10 cycles at 3.0 V and 0.0 V are shown in Fig. 6d and e. A comparison of these two patterns reveals that the difference is the broad peaks for Li_xSn , which are apparently not present in the pattern collected at 3.0 V. Additionally, the pattern shown in Fig. 6e is almost the same as the pattern in Fig. 6c. This figure shows that only the lithiation reaction of nano-scale tin particles that are embedded into a stable amorphous Li_3PO_4 matrix occurs during the charge and discharge process. It is noteworthy that, in a previous work reported by French [33], metallic tin was detected in the fully discharged products of $\text{LiSn}_2(\text{PO}_4)_3$. However, only Li_xSn was found in the fully discharged products in our experiment, which is mainly because of the nano-size of the precursors that reduce the bulk resistivity of material and makes it easier for the product to be fully lithiated.

To gain a better understanding of the kinetic mechanism of Li ion transportation in the electrode materials, electrochemical impedance spectroscopy (EIS) was employed at various voltages. $\text{LiSn}_2(\text{PO}_4)_3$ was used as the working electrode, and metallic lithium foil was used as the counter and reference electrodes. As shown in Fig. 7, the EIS collected at the open circuit voltage (OCV) is

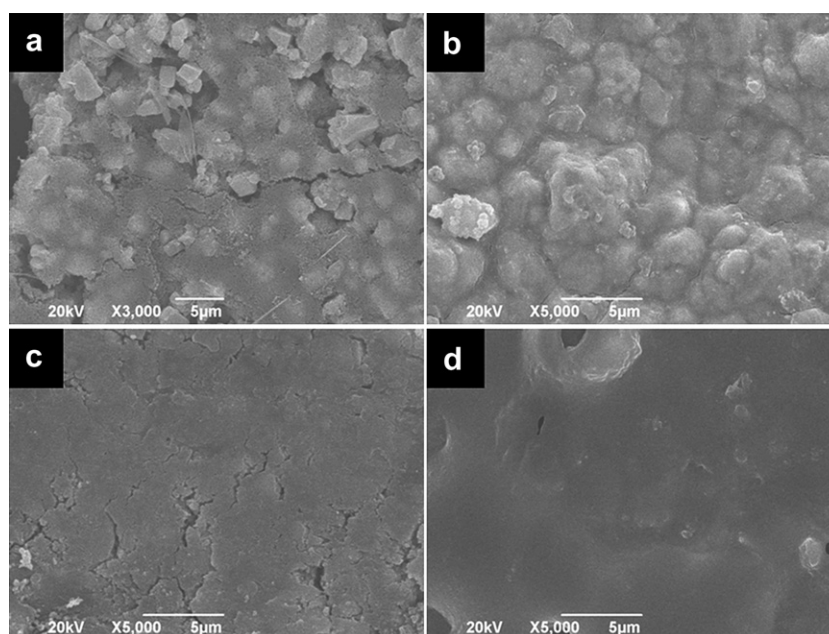


Fig. 5. SEM images of the surface morphologies of the prepared $\text{LiSn}_2(\text{PO}_4)_3$ electrode film after several charge and discharge cycles. (Fig. 5a, as-prepared $\text{LiSn}_2(\text{PO}_4)_3$ film, Fig. 5b, 5c, and 5d shows the film after 2, 10, and 50 cycles, respectively).

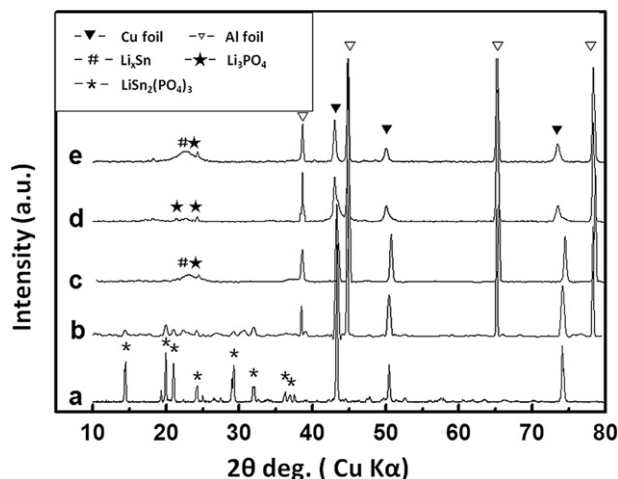


Fig. 6. Ex-situ XRD diffraction patterns of $\text{LiSn}_2(\text{PO}_4)_3$ at various charge/discharge states. (a. undischarged, b. after first discharge to 1.0 V, c. after first discharge to 0.0 V, d. after 10th charge to 3.0 V, and e. after 10th discharge to 0.0 V).

a semicircle at high frequency and a straight line at low frequency, which corresponds to a typical Li ion blocking process. When the cell is discharged to 1.0 V, the only change in the EIS is the increase in the diameters of the semicircle at high frequency. According to the widely accepted explanation, this increase is attributed to the interface resistance, which comes from partial SEI (solid electrolyte interface) and the formation of the Li_3PO_4 matrix, and the straight line is caused by the bulk Li ion diffusion process [34,35]. The EIS obtained at 0.0 V during the first discharge and the 10th discharge exhibit a new semicircle at a middle frequency. From consideration of the possible reactions at this potential, it is believed that the lithium alloying with freshly formed tin is responsible for these semicircles. The slight decrease in the semicircle diameter shown in Fig. 7d is probably due to the more compact Li_3PO_4 matrix and better contact between the particles after cycling. These results indicate that Li_3PO_4 is a stable matrix during the electrochemical process and guarantees that the tin particles are well dispersed during the reversible charge/discharge.

3.3. Lithium ion diffusion coefficient of $\text{LiSn}_2(\text{PO}_4)_3$

The diffusion coefficient (D_{Li}) expresses information on the kinetics and thermodynamics of the electrode process and mass

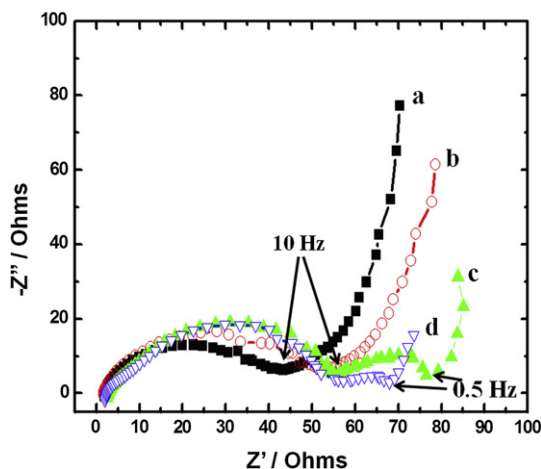


Fig. 7. Nyquist plots for a $\text{LiSn}_2(\text{PO}_4)_3/\text{Li}$ cell at different voltages: (a) OCV; (b) 1st discharge to 1.0 V; (c) 1st discharge to 0.0 V; (d) 10th discharge to 0.0 V.

transport [36]. To eliminate the influence of the binder and the electronic conductivity, the powder microelectrode cyclic voltammetry (CV) technique was used to determine the Li ion diffusion coefficient. CV tests were performed at various scan rates (0.1, 0.2, 0.5, 1, and 2 mV s^{-1}) in 1 M LiPF_6 EC/DMC/DEC electrolyte, and the scanning potential ranges were set between 0 and 2.0 V vs Li^+/Li . Because of the inconvenience caused by the irreversible process during the first cycle, only the second cycles using various scan rates were recorded, as shown in Fig. 8. A pair of redox peaks clearly appeared in every curve, which is attributed to the lithiation/delithiation process of tin. The details of the CV profile are illustrated in Fig. 9a and b, which show a liner relationship between $|E_p - E^0|$ and $\log v$ (the values of $|E_p - E^0|$ are calculated as half the difference between the potential peak values in the anodic and the cathodic sides, and the value of $|E_p - E^0|$ obtained is larger than 28 mV at all of the examined rates) and between i_p and $v^{1/2}$, where E_p is the peak potential, E^0 is the formal potential, v is the scan rate and i_p is the peak current. These results indicate that the lithiation/delithiation process of tin phosphate could be regarded as an irreversible electrochemical reaction [37].

For an irreversible process, the following equations are commonly used to calculate the D_{Li} :

$$i_p = 2.99 \times 10^5 (\alpha n)^{1/2} A \Delta C D_{\text{Li}}^{1/2} v^{1/2} \quad (25^\circ\text{C}) \quad (5)$$

$$|E_p - E^0| = \left(\frac{RT}{\alpha n F} \right) \left[0.780 + \ln \left(\frac{D_{\text{Li}}^{1/2}}{k^0} \right) + \ln \left(\frac{\alpha n F v}{RT} \right)^{1/2} \right] \quad (6)$$

where E_p , E^0 , v and i_p are as mentioned above, α is the transfer coefficient, n is the number of electrons involved in the rate-determining step and k^0 is the standard rate constant (cm s^{-1}).

According to Eq. (5), D_{Li} can be obtained from the slope of a plot of i_p vs $v^{1/2}$ with the knowledge of transfer coefficient, α , and the change in the Li-ion concentration ΔC . Because of the small current of the microelectrode, the potential drop caused by the uncompensated resistance, iR_u , has no effect on our measurement. The value of the transfer coefficient, α , and ΔC can be estimated from the slope of the line in Fig. 9a and b, according to Eqs. (5) and (6).

Assuming that the cavity of the microelectrode is a cylinder and that the particles inside the cavity are in closely packed structures with an interspaced rate of 25.9%, the volumes are estimated to be

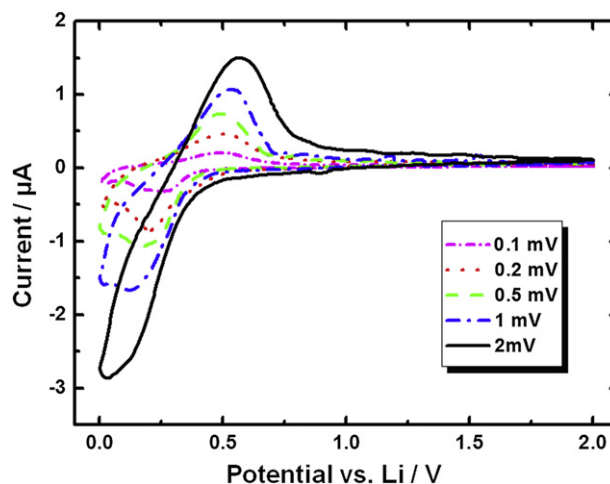


Fig. 8. Cyclic voltammograms at various sweep rates (0.1 mV s^{-1} , 0.2 mV s^{-1} , 0.5 mV s^{-1} , 1 mV s^{-1} , 2 mV s^{-1}) for the microelectrode of $\text{LiSn}_2(\text{PO}_4)_3$ in an organic electrolyte.

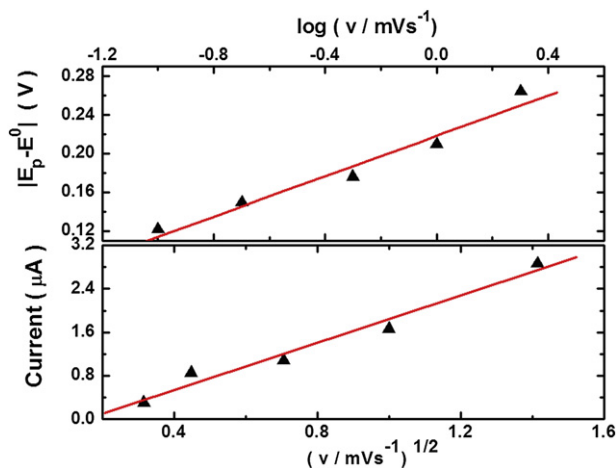


Fig. 9. $|E_p - E^0|$ vs. $\log v$ plots and peak current i_p vs. $v^{1/2}$ plots. Values of $|E_p - E^0|$ were calculated as half the difference between the anodic peak and cathodic peak potential from curve in Fig. 8.

$3.925 \times 10^{-8} \text{ cm}^3$ for the cavity and $2.908 \times 10^{-8} \text{ cm}^3$ for total particles (V_{total}), respectively. The average diameter of the particle (denoted as l) is estimated to be $0.9 \mu\text{m}$, as shown in Fig. 3c. The electrode area, A , is calculated to be $1.94 \times 10^{-3} \text{ cm}^2$ from $A = 4n\pi(l/2)^2$ (n is the number of particles in the electrode and is derived from $n = V_{\text{total}}/V_{\text{particle}}$). Therefore, $A\Delta C$ equals $1.39 \times 10^{-5} \text{ mol cm}^{-1}$. In Fig. 9b, the peak currents, i_p , increase with $v^{1/2}$ and exhibit good linearity. Therefore, the slope could be easily identified. Consequently, the value of the apparent D_{Li} for $\text{LiSn}_2(\text{PO}_4)_3$ is calculated to be $9.02 \times 10^{-13} \text{ cm}^2 \text{ s}^{-1}$. This value is close to the reported value in a previous study [38], which agrees with our hypothesis that the existence of the Li_3PO_4 matrix with a high Li ion diffusion coefficient has no influence on the Li ion diffusion in the active tin component. Additionally, the Li_3PO_4 matrix provides steady ion channels and maintains the integrity of electrode structure during cycling. This is the key factor for realizing the good electrochemical performance of $\text{LiSn}_2(\text{PO}_4)_3$.

3.4. Thermal stability of $\text{LiSn}_2(\text{PO}_4)_3$

Controlling the thermal runaway problem of the cell is considered a crucial technology in the commercial use of Li-ion batteries.

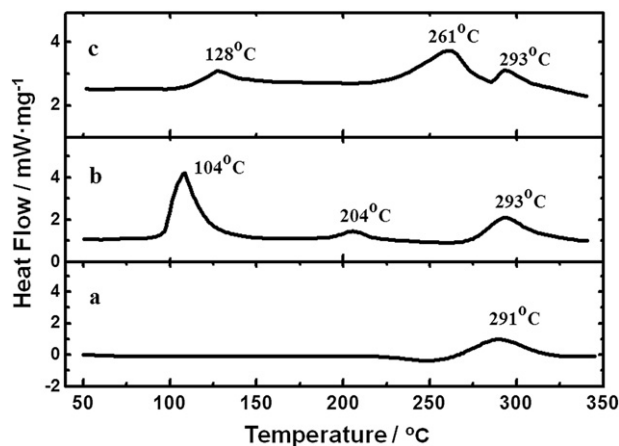
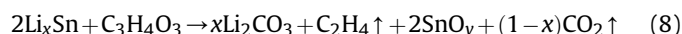
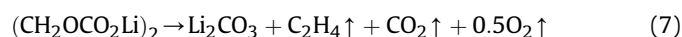


Fig. 10. DSC measurements of various samples at fully lithiated states with LiPF_6 in EC/DMC/DEC as the electrolyte (LB303). (a. LB303, b. Sn, c. $\text{LiSn}_2(\text{PO}_4)_3$, in N_2 flow at a heating rate of $10^\circ\text{C min}^{-1}$).

It is now widely accepted that phosphate-based materials have excellent thermal stability, and they have been regarded as potential safety battery materials for electric vehicles [39]. Herein, the thermal stability of $\text{LiSn}_2(\text{PO}_4)_3$ was investigated using DSC (Differential Scanning Calorimetry) measurements, and the results are presented in Fig. 10. The common commercial electrolyte consists of EC/DMC/DEC (1:1:1 by volume), and LiPF_6 was first tested, as shown in Fig. 10a. There is no obvious reaction until the temperature rises to 250°C . The broad exothermic peak that spreads from 250°C to 325°C corresponds to the decomposition of LiPF_6 with the formation of LiF and PF_5 . In contrast, the DSC curve acquired from fully lithiated, pure tin exhibits two significant exothermic peaks, from 95°C to 140°C and from 200°C to 220°C . According to a previous study, these two peaks are related to the breakdown of the SEI at lower temperatures, and the reaction between Li_xSn and the electrolyte after the SEI decomposition at higher temperatures [40]. The reactions are summarized in the following equations:



Similar to Fig. 10b, Fig. 10c shows the DSC curve that was obtained from the fully lithiated $\text{LiSn}_2(\text{PO}_4)_3$. However, the two peaks that appear in the DSC curve in Fig. 10c have higher beginning temperatures at 104°C and 215°C compared with the curve in Fig. 10b, which suggests the fact that $\text{LiSn}_2(\text{PO}_4)_3$ has higher thermal stability than pure Sn. The Li_3PO_4 matrix seems to play an important role in this improvement.

4. Conclusions

In summary, we have systematically studied the synthesis and electrochemical process of $\text{LiSn}_2(\text{PO}_4)_3$. A NASICON-structured $\text{LiSn}_2(\text{PO}_4)_3$ using nano- SnO_2 as a precursor was prepared at 900°C , with particle sizes of approximately $0.9 \mu\text{m}$, using a typical solid-state method. Compared to SnO_2 , this material exhibits better cycling performance, with a capacity of 320 mAh g^{-1} after 50 cycles. To gain a better understanding of such an improvement, a process that consists of the formation of a Li_3PO_4 matrix and the lithiation of tin particles has been confirmed using ex-situ XRD and EIS tests. Meanwhile, the apparent Li ion diffusion coefficient (D_{Li}) of $9.02 \times 10^{-13} \text{ cm}^2 \text{ s}^{-1}$ was calculated using the powder micro-electrode CV technique. Additionally, the DSC measurements suggest excellent thermal stability of $\text{LiSn}_2(\text{PO}_4)_3$. These results reveal the fact that the improved cycling performance of $\text{LiSn}_2(\text{PO}_4)_3$ is due to the Li_3PO_4 matrix, which can better limit the volume change and prevent the aggregation of tin clusters during cycling. This work also offers a potential phosphate-based tin anode for a safer battery and helps us better understand the relationship between matrix materials and electrochemical performance.

Acknowledgements

This work was partially supported by the National Natural Science Foundation of China (20925312), the State Key Basic Research Program of PRC (2011CB935903), and Shanghai Science & Technology Committee (10JC1401500, 377 08DZ2270500).

References

- [1] J.M. Tarascon, M. Armand, Nature 414 (2001) 359.
- [2] J.B. Goodenough, Y. Kim, Chem. Mater. 22 (2010) 587.
- [3] A.S. Arico, P.G. Bruce, B. Scrosati, J.M. Tarascon, W. van Schalkwijk, Nat. Mater. 4 (2005) 366.

- [4] P. Poizot, S. Laruelle, S. Grugeon, L. Dupont, J.M. Tarascon, *Nature* 407 (2000) 496.
- [5] Y. Idota, A. Matsufuji, Y. Maekawa, T. Miyasaka, *Science* 276 (1997) 1395.
- [6] Y. Idota, M. Nishima, Y. Miyaki, T. Kubota, T. Miyasaka, *Eur. Pat. Appl.* 651 (1995) 450.
- [7] M. Nagayama, T. Morita, H. Ikuta, M. Wakihara, M. Takano, S. Kawasaki, *Solid State Ionics* 106 (1998) 33.
- [8] A.D.W. Todd, P.P. Ferguson, M.D. Fleischauer, J.R. Dahn, *Int. J. Energy Res.* 34 (2010) 535.
- [9] J. Hassoun, S. Panero, G. Mulas, B. Scrosati, *J. Power Sources* 171 (2007) 928.
- [10] H. Mukaibo, A. Yoshizawa, T. Momma, T. Osaka, *J. Power Sources* 60 (2003) 119.
- [11] J.I. Yamaki, S.I. Tobishima, K. Hayashi, K. Sato, Y. Nemoto, M. Arakawa, *J. Power Sources* 74 (1998) 219.
- [12] J.J. Zhang, Y.Y. Xia, *J. Electrochem. Soc.* 153 (2006) A1466.
- [13] I.A. Courtney, J.R. Dahn, *J. Electrochem. Soc.* 144 (1997) 2045.
- [14] Y.W. Xiao, J.Y. Lee, A.S. Yu, Z.L. Liu, *J. Electrochem. Soc.* 146 (1999) 3623.
- [15] I.A. Courtney, J.R. Dahn, *J. Electrochem. Soc.* 144 (1997) 2943.
- [16] I.A. Courtney, W.R. McKinnon, J.R. Dahn, *J. Electrochem. Soc.* 146 (1999) 59.
- [17] J.K. Feng, H. Xia, M.O. Lai, L. Lu, *J. Phys. Chem. C* 113 (2009) 20514.
- [18] M. Behm, J.T.S. Irvine, *Electrochim. Acta* 47 (2002) 1727.
- [19] H.M. Xiong, W.Z. Shen, Z.D. Wang, X. Zhang, Y.Y. Xia, *Chem. Mater.* 18 (2006) 3850.
- [20] Y. Kim, H.H. Wang, K. Lawler, S.W. Martin, J. Cho, *Electrochim. Acta* 53 (2008) 5058.
- [21] H.Y. Wang, M. Yoshio, *Electrochem. Commun.* 8 (2006) 1481.
- [22] M. Wilkening, V. Epp, A. Feldhoff, P. Heitjans, *J. Phys. Chem. C* 112 (2008) 9291.
- [23] P. He, X. Zhang, Y.G. Wang, L. Cheng, Y.Y. Xia, *J. Electrochem. Soc.* 155 (2008) A144.
- [24] C. Gejke, L. Borjesson, K. Edstrom, *Electrochem. Commun.* 5 (2003) 27.
- [25] A. Martinez, J.M. Rojo, J.E. Iglesias, J. Sanz, R.M. Rojas, *Chem. Mater.* 6 (1994) 1790.
- [26] A. Martinez, J.M. Rojo, J.E. Iglesias, J. Sanz, *Chem. Mater.* 5 (1995) 1857.
- [27] N. Du, H. Zhang, J. Chen, J. Sun, B. Chen, D. Yang, *J. Phys. Chem. B* 112 (2008) 14836.
- [28] G. Ceder, Y.M. Chiang, D.R. Sadoway, M.K. Aydinol, Y.I. Jang, B. Huang, *Nature* 392 (1998) 694.
- [29] H. Yamamoto, M. Tabuchi, T. Takeuchi, H. Kageyama, O. Nakamura, *J. Power Sources* 68 (1997) 397.
- [30] A.M. Juarez, C. Pecharroman, J.E. Iglesias, J.M. Rojo, *J. Phys. Chem. B* 102 (1998) 372.
- [31] J.R. Dahn, I.S. Courtney, O. Mao, *Solid State Ionics* 111 (1998) 289.
- [32] I.S. Courtney, J.S. Tse, O. Mao, J. Hafner, J.R. Dahn, *Phys. Rev. B* 58 (1998) 23.
- [33] C.M. Burba, R. Frech, *J. Electrochem. Soc.* 152 (2005) A1233.
- [34] E. Pollak, G. Salitra, V. Baranchugov, D. Aurbach, *J. Phys. Chem. C* 111 (2007) 11437.
- [35] R. Ruffo, S.S. Hong, C.K. Chan, R.A. Huggins, Y. Cui, *J. Phys. Chem. C* 113 (2009) 11390.
- [36] H. Kanoh, Q. Feng, Y. Miyai, K. Ooi, *J. Electrochem. Soc.* 142 (1995) 702.
- [37] A.J. Bard, L.R. Faulkner, *Electrochemical Methods Fundamentals and Applications*, Wiley, New York, 2001, p. 160.
- [38] J.J. Zhang, P. He, Y.Y. Xia, *J. Electroanal. Chem.* 624 (2008) 161.
- [39] P. Ping, Q.S. Wang, J.H. Sun, H.F. Xiang, C.H. Chen, *J. Electrochem. Soc.* 157 (2010) A1170.
- [40] C.C. Chang, S.J. Liu, J.J. Wu, C.H. Yang, *J. Phys. Chem. C* 111 (2007) 16423.